Computational Analysis of Transverse Sonic Injection in Supersonic Crossflow Using RANS Models

Vatsalya Sharma
Department of Mechanical and
Aerospace Engineering,
Indian Institute of Technology,
Hyderabad, Telangana 502205, India
e-mail: me12m14p000005@iith.ac.in

Vinayak Eswaran[1]
Professor
Department of Mechanical and Aerospace
Engineering,
Indian Institute of Technology,
Hyderabad, Telangana 502205, India
e-mail: eswar@iith.ac.in

Debasis Chakraborty
Directorate of Computational Dynamics,
Defence Research and Development Lab,
Hyderabad, Telangana 500028, India

Transverse injection at sonic speed from a rectangular slot into a supersonic crossflow is numerically explored with an indigenously developed parallel three-dimensional (3D) Reynold-averaged Navier–Stokes (RANS) solver for unstructured grids. The RANS models used for turbulence closure are the one-equation Spalart–Allmaras (SA) model and the two-equation shear stress transport (SST) model. For each model, the influence of compressibility corrections is assessed. Due to the presence of shock-turbulent boundary layer interaction (STBLI) in the flow, various STBLI corrections are assessed for both the models. Most of the simulations are two-dimensional (2D), but three-dimensional simulations are also performed to investigate the mismatch between the experimental dataset and the numerical results. The SA model is less sensitive to STBLI corrections, but some improvement in its prediction of the separation distance is found with the compressibility corrections. The SST model results are insensitive to the compressibility corrections, but the STBLI correction improves its results. Improved agreement with the experimental dataset is found when simulations are done in 3D, suggesting that the experiments were not so close to 2D as previously believed. [DOI: 10.1115/1.4045985]

1 Introduction

Shock turbulence boundary layer interaction (STBLI) is a phenomenon that is encountered quite frequently during the design of high-speed aero vehicles and propulsion systems. It causes high heating rates and flow separation. This interaction drastically alters the characteristics of a turbulent boundary layer due to the presence of the adverse pressure gradients caused by the shocks. One situation where STBLI arises is seen when a jet is injected in the transverse direction at sonic speeds into a supersonic crossflow. This configuration is seen in supersonic ramjet engines and in thrust vector control devices for various high speed vehicles. Engineering predictions of the complex flow field for the design of aero-propulsion vehicles and systems usually rely on the Reynold-averaged Navier–Stokes (RANS) for turbulence closure. Large eddy simulations [1–5] and direct numerical simulations require a large number of grid points ($\approx$Re^3), which in turn makes the required computational resources and computing time exorbitant in such high Reynolds number flows. It is therefore important to find RANS models that produce reasonably accurate results with acceptable computational times.

The flow configuration of transverse sonic injection into the supersonic crossflow is quite simple, but the flow produces complex STBLI, which makes it a good candidate for the assessment of different RANS models for design and analysis of high-speed aero vehicles. Any RANS solver that is developed for application in the design of high-speed aero-propulsion vehicles requires STBLI-validated turbulence models. When a transverse flow comes through a slotted nozzle into the supersonic crossflow, its blockage of the freestream by the secondary flow causes the formation of strong bow shocks and a Mach disk, while the boundary layer separates [6]. Beyond the injection point, the boundary layer reattaches and a recompression shock wave is generated. The

presence of boundary layer separation and the Mach disk makes the flow very complex both upstream and downstream of the injection point. The two-dimensional (2D) flow field by Aso et al. [7] using a slot injection captures most of the flow features as seen in the three-dimensional (3D) flow field, as shown in Fig. 1.

Transverse jet injection at sonic speed from a flat plate into a supersonic crossflow has been extensively studied in the literature [8–10]. Several RANS models have been assessed by various researchers using the dataset from Aso et al. [7]. Parameters such as the upstream reattachment length (L_{up}) and jet-to-crossflow static pressure ratio characterize this flow field. Rizetta [11] performed two-dimensional numerical simulations of experiments of Aso et al. [7] using the k–ϵ model with compressibility corrections. He found that these calculations overpredict the pressure jump at the slot. Chenault and Beran [12] assessed the Reynolds stress transport model (RSTM) against the k–ϵ model. Two equation models do not account for anisotropy in Reynold's stresses; hence, it was expected for RSTM to provide better results. But the researchers [12] concluded that the expected improvements are not obtained from the RSTM model. They suggested that the
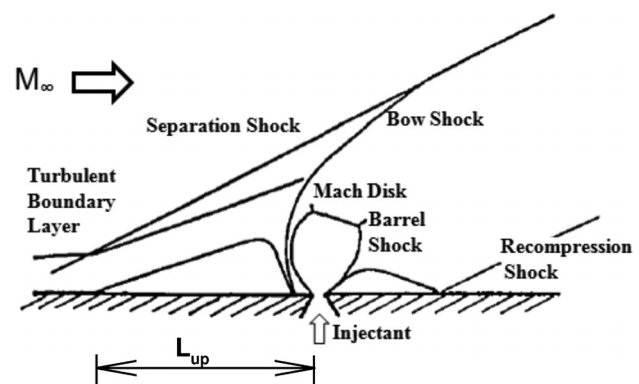

Fig. 1 Schematic diagram of flow field through transverse slotted injection in supersonic crossflow as given by Aso et al. [7]

RANS models could be inherently inadequate at such high speed and pressure ratios but also mentioned that the differences between the boundary conditions between experiments and simulation could be a possible cause of error.

Sriram and Mathew [13] used the k–ω model with the Roe and the MUSCL schemes for the 2D flow field. They found slight improvements in the results using a higher order scheme, and noted that if careful attention is paid to the mesh refinement near the injector inlet and in the turbulent boundary layer, better results could be produced. But they still could not match the experiments as expected, although they found that the prediction with k–ω is comparable with the RSTM results of Chenault and Beran [12]. As the STBLI are highly unsteady in nature, and this is not accounted for by the RANS models, the researchers thought this could be a major cause for the mismatch with the experiments.

Huang et al. [14] and Yan et al. [15] studied various turbulence models using a commercial solver, and concluded that different models work well at different pressure ratios. The numerical results obtained in these studies, however, still reflect the differences with the experiment seen by the previous researches [11–13]. It is seen that a more accurate match is obtained for lower pressure ratios, with the disagreement increasing with the increase in pressure ratio. Their results exhibit a clear problem with the shear stress transport (SST) model in obtaining accurate results. Even changing the freestream flow conditions [16] or the nozzle geometry [17,18] does not change the discrepancies in the results obtained with the aforementioned RANS models. Three-dimensional simulations for the same problem have been reported by Huang [19] and Huang et al. [20] using the SST model. They show a mismatch in their validations, the source of which may lie in the lack of true two dimensionality of the experiments, but also perhaps because these authors did not consider the STBLI and stagnation point effects in their simulations.

The one-equation Spalart–Allmaras (SA) [21] has become popular for its reasonably accurate predictions of a wide range of aerodynamic flow problems [22], even in comparison with the two-equation based RANS turbulence models, while being computationally inexpensive. However, an extensive study based on the one-equation Spalart–Allmaras model with and without compressibility correction still remains to be done to establish its application for STBLI flow fields. The SST model proposed by Menter [23] is a combination of standard k–ϵ and k–ω models and combines the best from both the models in far-field and near-wall behavior. This model is widely used for aerodynamics flows, as it captures the boundary layer better than the k-ϵ model and is free from the sensitivity to the freestream turbulence levels seen in the k–ω model. This model gives good agreement with the experimental data for adverse pressure gradient boundary-layer flows.

A major disadvantage of two-equation RANS models is the overprediction of the turbulence energy in the vicinity of stagnation points. In order to avoid the buildup of turbulent kinetic energy (TKE) in these regions, the production term in the TKE equation can be limited for which corrections have been proposed by Menter [24] and Kato-Launder [25]. As mentioned, STBLI is highly unsteady in nature [26] and this is not for those accounted by RANS models. Sinha et al. [27] assessed and established [28] that there is unphysical overproduction of TKE by RANS models due to STBLI. They reasoned that the unsteady motion of a shock results in a mean shock thickness that is much larger than that of a steady shock at the same mean-flow conditions. So, they derived an alternate way of predicting the turbulence production in the TKE equation. Given its lack of a TKE equation, it will be interesting to see the behavior of the Spalart–Allmaras model for STBLI with the correction suggested by Sinha et al. [29]. However, the common practice in the literature is that most researchers use the standard RANS models without any kind of correction for the unsteady nature of STBLI.

An unstructured grid parallel three-dimensional RANS all speed solver has been developed in-house to solve flow problems of low to high Mach number by the present authors [30]. This newly developed solver is used with the SA and SST models with and without compressibility and STBLI corrections to simulate the experimental conditions of Aso et al. [7] to benchmark the in-house solver for aero-propulsion applications. Although most of the simulations are two-dimensional, three-dimensional simulations have also been done to assess the effect of three-dimensionality in the experiments. The effect of pressure ratios and slot widths on flow development is investigated and the computed results are compared with the experimental data. Hence, in this paper, these two models of different philosophies have been assessed with different corrections for application in the STBLI-dominated flows.

2 Numerical Method

The details of the in-house parallel three-dimensional unstructured grid RANS solver for all speeds are given in this section.

2.1 Governing Equation. The density-based finite volume solver uses a low-speed preconditioned form of the Navier–Stokes equation [31] that allows its use for both the compressible and incompressible flow regimes. The solver can handle three-dimensional unstructured grids in computational fluid dynamics (CFD) general notification system format. The equation of state for an ideal gas is used

$$p = \rho R T \qquad (1)$$

where ρ, T, and P are the density, temperature, and pressure of the fluid, respectively, and R is the ideal gas constant for air, taken as 287 $\text{JKg}^{-1}\text{K}^{-1}$. The velocity vector is defined as

$$\mathbf{V} = u\hat{\mathbf{i}} + v\hat{\mathbf{j}} + w\hat{\mathbf{k}} \qquad (2)$$

The integral form of the Navier–Stokes equation with control volume V and elemental face area $\mathbf{d}S$ is given as

$$\frac{\partial}{\partial t}\int_V \boldsymbol{W}\, dV + \oint [\boldsymbol{F} - \boldsymbol{G}] \cdot d\boldsymbol{A} = \int_V \boldsymbol{H}\, dV \qquad (3)$$

where $\boldsymbol{W}$ represents the conservative variables vector

$$\boldsymbol{W} = \{\rho, \rho u, \rho v, \rho w, \rho E\}^T \qquad (4)$$

The magnitude of the face area $\mathbf{S}_f$ is A_f and its unit vector is $\hat{\mathbf{n}}_f$. In the governing equation (Eq. (12)), $\boldsymbol{G}$ is the diffusion vector and $\boldsymbol{F}$ is the convective vector of the compressible Navier–Stokes equation which are defined as

$$\mathbf{F} = \begin{Bmatrix} \rho \mathbf{V} \\ \rho \mathbf{V}u & +P\hat{\mathbf{i}} \\ \rho \mathbf{V}v & +P\hat{\mathbf{j}} \\ \rho \mathbf{V}w & +P\hat{\mathbf{k}} \\ \rho \mathbf{V}E & +P\mathbf{V} \end{Bmatrix}, \quad \mathbf{G} = \begin{Bmatrix} 0 \\ \tau_{xi} \\ \tau_{yi} \\ \tau_{zi} \\ \tau_{ij}\mathbf{V}_j + \mathbf{q} \end{Bmatrix} \qquad (5)$$

Here, E and H are, respectively, the total energy and total enthalpy per unit mass

$$E = H - \frac{p}{\rho}; \quad H = h + |\mathbf{V}|^2/2 \qquad (6)$$

and $\mathbf{q}$ is the heat flux vector

$$\boldsymbol{q} = -k'\frac{\partial T}{\partial x_j} \qquad (7)$$

where k' is the thermal conductivity of the fluid and τ is the viscous stress tensor

$$\tau_{ij} = -P\delta_{ij} + \mu_L\left(\frac{\partial U_i}{\partial x_j} + \frac{\partial U_j}{\partial x_i}\right) + \lambda(\mathrm{div}\mathbf{V})\delta_{ij} \qquad (8)$$

where λ is the coefficient of bulk viscosity, determined using Stoke's hypothesis [32]

$$\lambda + \frac{2}{3}\mu_L = 0 \qquad (9)$$

and μ_L is the laminar dynamic viscosity of the fluid. In order to obtain accurate solutions for both compressible and incompressible flows, low speed preconditioning given by Weiss and Smith [31] is implemented in the solver. The low-speed preconditioning matrix (Γ) is given as

$$\Gamma = \begin{bmatrix} \Theta & 0 & 0 & 0 & \rho_T \\ \Theta u & \rho & 0 & 0 & \rho_T u \\ \Theta v & 0 & \rho & 0 & \rho_T u \\ \Theta w & 0 & 0 & \rho & \rho_T u \\ \Theta H - \delta & \rho u & \rho v & \rho w & \rho_T H + \rho C_p \end{bmatrix} \qquad (10)$$

where

$$\Theta = \left(\frac{1}{U_r^2} - \frac{\rho_T}{\rho C_p}\right), \quad \rho_p = \frac{\partial \rho}{\partial P}\bigg|_T, \quad \rho_T = \frac{\partial \rho}{\partial T}\bigg|_P \qquad (11)$$

This transforms the governing equation given by Eq. (3) to

$$\Gamma\frac{\partial}{\partial t}\int_V \mathbf{Q}\,dV + \oint[\mathbf{F} - \mathbf{G}]\cdot d\mathbf{G} = \int_V \mathbf{H}\,dV \qquad (12)$$

where $\mathbf{Q}$ is the primitive variables vector given as

$$\mathbf{Q} = \{P, u, v, w, T\}^T \qquad (13)$$

In Eq. (11), U_r is the reference velocity and δ is a constant of preconditioning, whose definitions can be found in Weiss et al. [33]. The vector $\boldsymbol{H}$ in Eqs. (3) and (12) contains source terms for body forces and energy sources, which have been set as 0 in this paper. The second-order Roe scheme [34], preconditioned for low speeds [33], has been used for modeling the convective vector $\boldsymbol{F}$ of the governing equation with the Venkatakrishnan limiter [35,36]. The gradients in the diffusion vector $\boldsymbol{G}$ are computed using the Green–Gauss cell-based method. Explicit time stepping is used to march to the solution using the fourth-order Runge–Kutta method [37] on the governing equations as

$$\frac{\partial \boldsymbol{Q}}{\partial t} = \mathbf{R}^i \qquad (14)$$

where the suffix i denotes the ith step of the Runge–Kutta method. The time-step Δt is computed from the Courant–Friedrichs–Lewy (CFL) condition

$$\Delta t = \frac{2\mathrm{CFL}\cdot V}{\sum_f \lambda_f^{\max} A_f} \qquad (15)$$

where V is the cell volume, A_f is the area of each face of the cell, and CFL is a prescribed value below unity. We calculate $\lambda_f^{\max}$ as given by Blazek [38]. The same time-step is used in each cell of the domain. The residue e of each variable solved is stored and is checked for convergence independently

$$e = \sqrt{\frac{1}{\Delta t}\sum_{\mathrm{cells}}(\boldsymbol{Q}^{n+1} - \boldsymbol{Q}^n)} \qquad (16)$$

As part of preprocessing, five iterations are performed. Out of these five iterations, the maximum residual for each variable is retained. Then using this maximum residual, we compute the normalized residual for the rest of the solution by

$$e_{\mathrm{final}} = \frac{e}{e_{\max,5}} \qquad (17)$$

Normalization ensures that the initial residuals for all equations are of $O(1)$ which is quite useful in judging overall convergence.

2.2 Turbulence Modeling. The Spalart–Allmaras and the SST models are used in this study along with various corrections proposed by previous researchers. The Boussinesq assumption is used for modeling the Reynolds' stress τ_{ij} as

$$\tau_{ij} = 2\mu_t\left(S_{ij} - \frac{1}{3}\frac{\partial U_k}{\partial x_k}\delta_{ij}\right) - \frac{2}{3}\rho k\delta_{ij} \qquad (18)$$

where S_{ij} is the strain rate tensor given as

$$S_{ij} = \frac{1}{2}\left(\frac{\partial U_i}{\partial x_j} + \frac{\partial U_j}{\partial x_i}\right) \qquad (19)$$

and μ_t is the turbulent viscosity computed by using the turbulence model.

2.2.1 Spalart–Allmaras Model. The one-equation model proposed by Spalart and Allmaras [21] has been implemented in a low-Reynolds number form. The model computes the normalized eddy viscosity $\tilde{\nu}$ using the governing equation expressed in differential form as

$$\frac{\partial \tilde{\nu}}{\partial t} + \frac{\partial}{\partial x_i}(\tilde{\nu} U_i) = P_{\tilde{\nu}} - D_{\tilde{\nu}} + S_{\tilde{\nu}} \qquad (20)$$

The model constants and definitions are as given by Spalart and Allmaras [21].

2.2.2 Shear Stress Transport k–ω Model. The two-equation model of Menter [23] in its low Reynolds number form is implemented. The model equations implemented in the solver are

$$\frac{\partial(\rho k)}{\partial t} + \frac{\partial(\rho U_j k)}{\partial x_j} = P_k - \beta^*\rho\omega k + D_k \qquad (21)$$

$$\frac{\partial(\rho\omega)}{\partial t} + \frac{\partial(\rho U_j\omega)}{\partial x_j} = \gamma'\frac{\omega}{k}P_k - \beta\rho\omega^2 + D_\omega + AA \qquad (22)$$

where P_k is the production of turbulent kinetic energy, which is evaluated as

$$P_k = \tau_{ij}\frac{\partial U_j}{\partial x_i} \qquad (23)$$

The rest of the model constants and definitions are as given by Menter [23]. The distance from the wall is computed in the same manner as in the Spalart–Allmaras model [21]. The value of laminar Prandtl number is taken as 0.71 and the turbulent Prandtl number (Pr_T) is taken between 0.7 and 0.9.

2.2.3 Shock Boundary Layer Modifications. A major disadvantage of the two-equation RANS models is the overprediction of the turbulent kinetic energy in the vicinity of the stagnation points. In order to avoid the buildup of the TKE in these regions, the production term in the RANS governing equation can be artificially limited. The TKE production (P_k) given in Eq. (23) can be expanded as

$$P_k = \mu_t\left(2S_{ij}S_{ji} - \frac{2}{3}S_{ij}^2\right) - \frac{2}{3}\rho k S_{ii} \tag{24}$$

Several ways in which P_k can be limited have been suggested in the literature. The modified P_k shall be denoted as P'_k below. Kato-Launder [25] gave a correction to limit the production in the recirculation zone. This correction was to be applied for vortex shedding flow over square cylinders. It is given as

$$P'_k = \mu_t \Omega S \tag{25}$$

where Ω is the vorticity magnitude, given as $\Omega = \sqrt{2W_{ij}W_{ij}}$. Another prescription was given by Menter [23], where P_k can be limited by

$$P'_k = \min(P_k, 20\beta^*\rho\omega k) \tag{26}$$

Sinha et al. [27] studied the overproduction of the TKE for STBLI with direct numerical simulations data. The unsteady motion of shocks results in a much larger mean shock thickness. Across a shock wave, P_k is proportional to S_{ji}^2 which becomes very large in magnitude, resulting in excessively large values of k. They proposed a completely different P_k for RANS models given as

$$P'_k = -\frac{2}{3}\rho k S_{ii}\left(1 - b'_1\right) \tag{27}$$

where

$$b'_1 = \max\left[0, 0.4(1 - e^{1-M_{1n}})\right] \tag{28}$$

and M_{1n} is given as

$$M_{1n} = \frac{U.\nabla P}{a|\nabla P|} \tag{29}$$

Here, the value of a is the local speed of sound. For the SA model, where k is not computed, Sinha et al. [29] devised a correction based on the turbulent viscosity μ_t. The correction P_c is given as

$$P_c = C'_{b1}\rho\tilde{\nu}S_{ii} \tag{30}$$

where

$$C'_{b1} = \frac{4}{3}(1 - b') - \frac{2}{3}C_{\epsilon 1} \tag{31}$$

and $C_{\epsilon 1}$ is given as

$$C_{\epsilon 1} = 1.25 + 0.25(M_{1n} - 1) \tag{32}$$

This correction should be subtracted from $P_{\tilde{\nu}}$ in the governing equation. Hence, the final term $P'_{\tilde{\nu}}$ is given as

$$P'_{\tilde{\nu}} = P_{\tilde{\nu}} - P_c \tag{33}$$

which replaces $P_{\tilde{\nu}}$ in Eq. (20).

2.3 Compressibility Corrections for Turbulence Models

2.3.1 Spalart–Allmaras Model. Due to the absence of the turbulent Mach number in the Spalart–Allmaras model, the compressibility correction employed in the two-equation models [39] cannot be used. So, Paciorri and Sabetta [40] suggested corrections that relate mixing layer thickness to turbulent viscosity using the experimental correlation between the growth rate and the thickness. This is analogous to having dependence on turbulent Mach number but actually imposes direct dependence on the convective Mach number. The compressibility correction is

$$Y_C = -C_c\frac{\tilde{\nu}^2}{a^2}\frac{\partial U_i}{\partial x_i}\frac{\partial U_i}{\partial x_i} \tag{34}$$

where C_c is a constant whose value is determined as 3.5. This term is then added to the right side of the transport equation (Eq. (20)).

2.3.2 Shear Stress Transport Model. In order to model the compressibility effects in the k–ϵ model, Sarkar proposed additional source terms for the dilatation dissipation [41] and pressure dilatation [42] for the TKE equation. Wilcox [43] gives a procedure by which these corrections can be applied to the SST model. In order to include these compressibility corrections in the SST model, the constants β^* and β in the governing equations for SST model are modified as

$$\beta^* = \beta_0^*\left[1 + M_t^2\right] \tag{35}$$

$$\beta = \beta_0 - \beta_0^*M_t^2 \tag{36}$$

where the values of β_0^* and β_0 are the values of β^* and β given by Menter [23]. Here, M_t is the turbulent Mach number, given as

$$M_t = \frac{\sqrt{2k}}{a} \tag{37}$$

where a is the local speed of sound, given as

$$a = \sqrt{\gamma R T} \tag{38}$$

and k is the turbulent kinetic energy, T is the temperature, R is the universal gas constant, and γ is the ratio of specific heats, whose value is taken as 1.4 for air.

3 Numerical Validation and Verification of the Solver

In Secs. 3.1 and 3.2, the RANS solver is validated for benchmark cases to establish its capabilities and accuracy.

3.1 Turbulent Flow Over Flat Plate.
Turbulent flow over a flat plate of length 2 m with zero pressure gradient is computed for a freestream Mach number (M_∞) of 0.2 and a Reynolds number per unit length (Re_x) of 5×10^6.

The simulation domain with boundary conditions is given in Fig. 2. Boundary conditions are prescribed in primitive variables form. At the inlet, pressure inlet and turbulent conditions are prescribed with $(P_0/P_\infty) = 1.02828$ and $(T_0/T_\infty) = 1.0008$. For sections labeled as symmetry, $(\partial\mathbf{Q}/\partial n) = 0$ has been prescribed. The wall is assumed as adiabatic, so $\mathbf{U} = 0$, $(\partial T/\partial n) = 0$, $(\partial P/\partial n) = 0$, and $(\partial\tilde{\nu}/\partial n) = 0$ have been prescribed as boundary conditions there. At the outflow, $(P_0/P_\infty) = 1$ has been prescribed and the remaining quantities are taken from interior values. The boundary conditions for various turbulent models have been given in Table 1. For Dirichlet boundary condition, the values of k and ω are calculated using the value of turbulence intensity by using the formulae
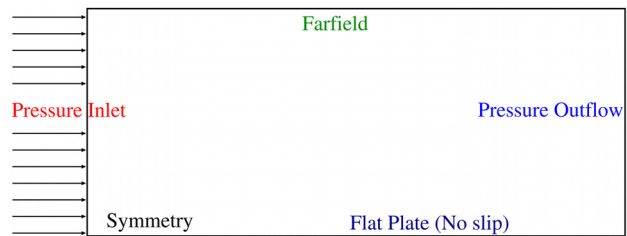

Fig. 2   Geometry for simulations and its boundary conditions

Table 1 Boundary conditions for turbulence variables

Section	SST	Spalart–Allmaras
Inlet	Dirichlet boundary condition	$\frac{\tilde{\nu}}{\nu_\infty} = 3.0$
Adiabatic wall	$k = 0 \; \omega = 0$	$\frac{\tilde{\nu}}{\nu_\infty} = 0.0$
Outlet	$\frac{\partial k}{\partial n} = 0 \; \frac{\partial \omega}{\partial n} = 0$	$\frac{\partial \tilde{\nu}}{\partial n} = 0$
Symmetry	$\frac{\partial k}{\partial n} = 0 \; \frac{\partial \omega}{\partial n} = 0$	$\frac{\partial \tilde{\nu}}{\partial n} = 0$
Farfield	Dirichlet boundary condition	$\frac{\tilde{\nu}}{\nu_\infty} = 3.0$

Table 2 GCI study for turbulent flat-plate case

Parameter	Value
N_1, N_2, N_3	51300, 12825, 2925
r_{21}	2.0
r_{32}	2.09
ϕ_1	0.0027283
ϕ_2	0.0027112
ϕ_3	0.0027067
p	1.96
ϕ_{ext}^{21}	0.0027056
e_a^{21}	0.1631%
GCI^{21}	0.052%
e_a^{32}	0.6342%
GCI^{32}	0.2034%

$$k = 1.5 I^2 U_{inlet}^2 \qquad (39)$$

$$\epsilon = C_\mu^{3/4} k^{3/2} l^{-1}; \quad \omega = \frac{\epsilon}{C_\mu k} \qquad (40)$$

where I is the level of turbulence intensity, U_{inlet} is the inlet velocity, and l is the integral length scale given as $l = 0.07 L$, with L being the characteristic length of the domain. The value of I is taken as 1% and L is taken as 2 m. Explicit time stepping with CFL numbers ranging from 0.1 to 0.9 are used for the simulation and the same steady-state result is obtained for all the CFL

numbers, showing a good temporal convergence. The solution is considered converged once the normalized velocity and pressure residuals are below 1×10^{-6} and turbulent variables' residuals are below 1×10^{-3}. Grid sensitivity study was checked with three grids using the grid convergence index (GCI) procedure [44]. The results obtained with these grids have been tabulated in Table 2.

The parameter used for the GCI is the wall skin friction coefficient (C_f), that has been referred to as ϕ in Table 2. N is the number of elements in each mesh, $r = \sqrt{(N_{coarse}/N_{fine})}$, and p is the apparent order of calculation. As $N_1 > N_2 > N_3$, e_a^{21} represents the estimated relative error and GCI^{21} is the fine grid convergence index, which gives the uncertainty in the value of the result on the finer mesh. It should be noted that, as the Spalart–Allmaras is a low Reynold's number model, near wall $y^+ < 1$ is required for all the grids. The grid is stretched in the wall-normal direction and is also clustered near the plate's leading edge. On the basis of GCI, the grid with 12,825 hexahedral cells is selected for the further computations.

Two key parameters are now compared with benchmark results to demonstrate the accuracy of the solver, namely, $u+$ against $y+$ (at Re$_\theta$=10,000) and wall skin friction coefficient (C_f) against Re$_\theta$ (for $4000 < $ Re$_\theta < 13{,}000$). Definitions are given by Carlson [45] for all the relevant quantities, including Re$_\theta$, C_f, u^+, and y^+. The results obtained from the solver are compared with the theoretical Karman–Schoenherr (K-S) relation [46] and Coles theory [47] which are shown in Figs. 3(a) and 3(b), respectively. Note that these particular theoretical correlations are not necessarily perfect, as they incorporate a wide range of experimental and numerical data. However, the present numerical results give a very good match in Figs. 3(a) and 3(b).

3.2 Supersonic Turbulent Flow Over Flat Plate. Using the computational domain and grid given in Sec. 3.1, supersonic turbulent flow over a flat plate is computed for a freestream Mach number (M_∞) of 2. The Reynolds number per unit length (Re$_x$) is taken as 15×10^6. The boundary conditions are prescribed in the primitive variables form. At the inlet, freestream conditions for all the variables are prescribed. For sections labeled as symmetry, $(\partial \mathbf{Q}/\partial n) = 0$ has been prescribed. The wall is assumed to be at constant temperature, with the wall-to-freestream temperature ratio being $(T_w/T_\infty) = 1.712$, where the subscript w denotes the wall and ∞ denotes the freestream. For the rest of the variables, $\mathbf{U} = 0$, $(\partial P/\partial n) = 0$, and $(\partial \tilde{\nu}/\partial n) = 0$ have been prescribed as the wall boundary conditions. At the outflow, all the quantities are extrapolated from interior values. The boundary conditions for various turbulent models have been given in Table 1.

In order to compare the computed u^+ and y^+ from simulations with the theoretical results, the incompressible law of the wall
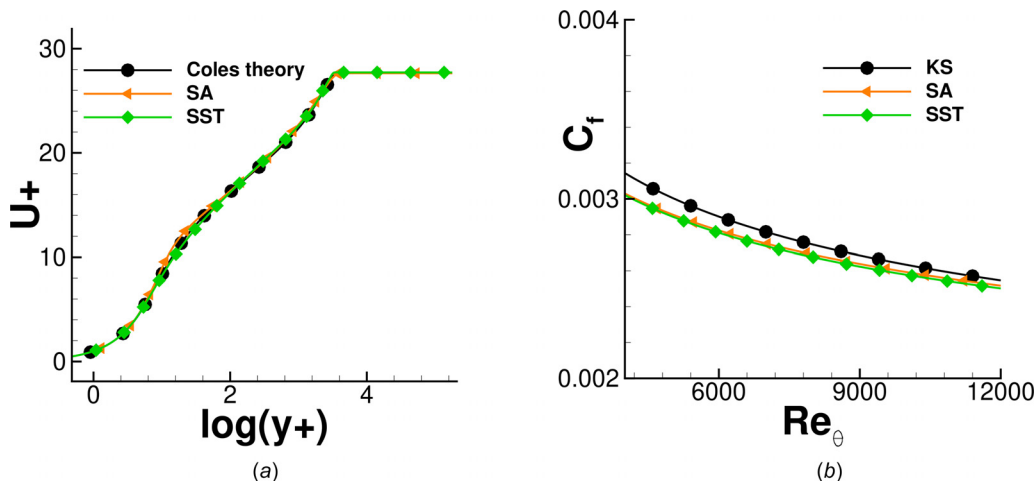

Fig. 3 Turbulent flatplate results using RANS models compared with benchmark results: (a) $u+$ versus $y+$ and (b) C_f versus Re$_\theta$
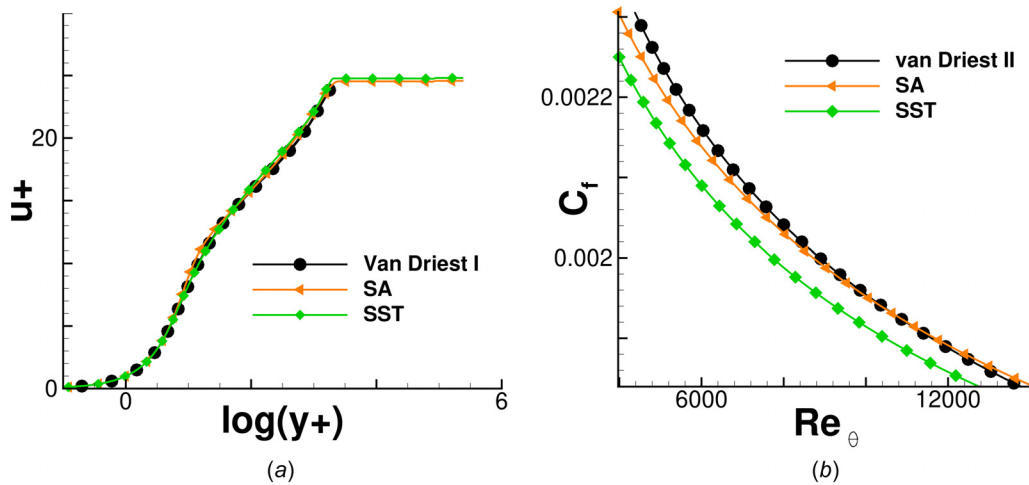
Fig. 4 Supersonic turbulent flow over a flatplate result using RANS models compared with benchmark results: (*a*) *u*+ versus *y*+ and (*b*) C_f versus Re$_\theta$
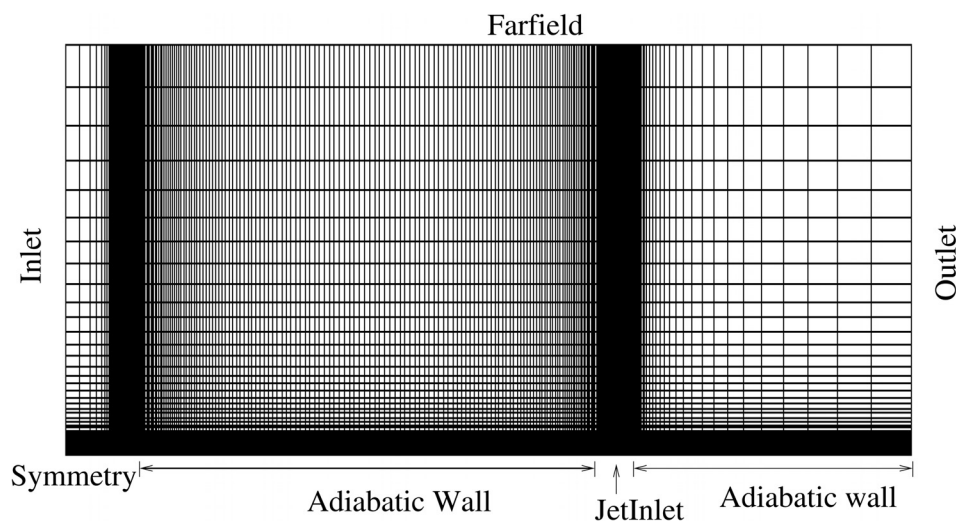

Fig. 5 Geometry for simulations and its boundary conditions

based on Coles' [47] mean velocity profile is used along with van Driest [48] type damping near the wall. In order that the incompressible law of the wall to be used for supersonic flow with a constant wall temperature, the van Driest I transformation [49] is applied. The final results are presented in Fig. 4(*a*). Theoretical correlation for C_f is obtained using the Karmen–Schoenherr relation [46]. This is transformed for application in compressible flow using the van Driest II transformation [48] and the results are presented in Fig. 4(*b*). It should be noted that, while the theoretical correlations are inexact, the numerical results give a good match in Figs. 4(*a*) and 4(*b*).

4 Application to Crossflow Injection to Supersonic Flow

4.1 Brief Details of the Experimental Conditions. The experimental study of the slot injection into a supersonic crossflow done by Aso et al. [7] has often been used as a benchmark study for numerical investigations. Gaseous nitrogen was injected into a supersonic freestream flow from a rectangular slot. The flat plate was placed horizontally in a supersonic wind tunnel of cross section 150 mm × 150 mm. The slot nozzle was placed 330 mm downstream from the leading edge of the flatplate. Experiments were conducted for a freestream Mach number of 3.75–3.81, total pressure of 1.20 MPa, and total temperature of 283 − 299 K. The Reynolds number based on the distance between the leading edge of the

flat plate and the centerline of the slot was between 1.03×10^7 and 2.07×10^7. In the experiments, P_∞ was kept constant, whereas the total pressure of flow injected from the slot $P_{0,inj}$ was varied between 0.1 MPa and 0.6 MPa to get different pressure ratios. The flow fields were visualized by Schlieren photography and the static pressures were measured using multitube manometers. The parameters presented in the experimental paper are the upstream reattachment distance (L_{up}), the normalized pressure distribution upstream and downstream of the jet outlet, and the height of the jet penetration into the crossflow. In the experiments, the crossflow enters the supersonic flow from a slot of width 70 mm. Aso et al. [7] provide two sets of data for each of the aforementioned parameters. The first set is putatively two-dimensional in nature, as the flow from the slot was stopped from turning around the edges of the slot by the use of an aerodynamic fence. This fence was thought by the experimenters to render the flow effectively 2D, even with the use of a finite slot. We shall show that this assumption is contestable. The second dataset is computed without the aerodynamic fences, hence the flow is three-dimensional. Now the results from two-dimensional simulations are presented and compared with the data from the first set. Thereafter, the 3D flow is also simulated.

4.2 Computational Domain. The computational domain with grid distribution and boundary conditions is shown in Fig. 5.

The meshes are made with the ICEM CFD software in CFD general notification system format. Unstructured meshes with quadrilateral elements at the boundary section and hexahedral elements in the inner computational section have been used. Since the solver is based on the finite volume method, meshes with unit width in the Z direction are used for the 2D computations, with symmetry conditions prescribed in the Z direction. A domain of size $(500 + W)$ mm $\times$ 150 mm is used for the numerical study, where W is the width of the jet inlet. The origin is taken at the center of the jet inlet. The length of plate before the injector is 330 mm and 150 mm after it, with an entrance section of 20 mm with symmetry boundary condition placed between the inlet and the wall. Sriram and Mathew [13] obtained better results by refining the mesh near the injector and keeping a significant number of nodes in the turbulent boundary layer. As seen in Fig. 5, the grid is clustered selectively at the jet inlet, near the wall region, and at the leading edge of the plate using a hyperbolic mesh law and by using an exponential mesh law in the lateral direction. At least 40% of the nodes in the transverse direction are concentrated in the region between wall and 7 W distance in the lateral direction. The subscript infinity (∞) denotes the freestream values. Table 3 presents the experimental values [7] which will be used for the simulations. As in the experiment, Nitrogen gas is assumed in the simulation and the Sutherland law of viscosity with the coefficients for Nitrogen is used [50]. The inlet boundary conditions are prescribed as pressure inlet boundary conditions, the values of which are given in Table 3. For the wall, $\mathbf{U} = 0$, $(\partial T/\partial n) = 0$, and $(\partial P/\partial n) = 0$ are prescribed. For the outflow, $(P_0/P_\infty) = 1$ is prescribed for pressure, with the remaining quantities being prescribed from the interior values. Since the injection is done at sonic speed, choked flow conditions at the jet inlet are prescribed, using a given inlet jet pressure ratio which is defined in Eq. (41). The Reynolds number based on the distance between the leading edge of the plate and the slot nozzle is taken as 2.07×10^7. The boundary conditions for various turbulent models are given in Table 4

$$P_{\text{ratio}} = \frac{P_{\text{jet}}}{P_\infty} \qquad (41)$$

$$P_{\text{norm}} = \frac{P_{\text{wall}}}{P_\infty} \qquad (42)$$

Table 3 Inlet flow conditions

Parameter	Value
M_∞	3.75
$P_{\text{total},\infty}$	1.20 MPa
$T_{\text{total},\infty}$	299 K

Table 4 Boundary conditions for turbulence variables

Section	SST	Spalart–Allmaras
Inlet	Dirichlet boundary condition	$\dfrac{\tilde{\nu}}{\nu_\infty} = 3.0$
Adiabatic wall	$k = 0 \ \omega = 0$	$\dfrac{\tilde{\nu}}{\nu_\infty} = 0.0$
Outlet	$\dfrac{\partial k}{\partial n} = 0 \ \dfrac{\partial \omega}{\partial n} = 0$	$\dfrac{\partial \tilde{\nu}}{\partial n} = 0$
Symmetry	$\dfrac{\partial k}{\partial n} = 0 \ \dfrac{\partial \omega}{\partial n} = 0$	$\dfrac{\partial \tilde{\nu}}{\partial n} = 0$
Jet inlet	$\dfrac{\partial k}{\partial n} = 0 \ \dfrac{\partial \omega}{\partial n} = 0$	$\dfrac{\partial \tilde{\nu}}{\partial n} = 0$
Farfield	Dirichlet boundary condition	$\dfrac{\tilde{\nu}}{\nu_\infty} = 3.0$

The simulations were carried out on an Intel Xeon central processing unit number X5680 at 3.33 GHz with 24 processors. Mesh division for parallel processing was done using Metis for message passing interface-based parallel simulations. Explicit time stepping with CFL numbers ranging from 0.1 to 0.4 is taken for the simulations. At all the CFL numbers between 0.1 and 0.4, same steady-state P_{norm} profile is achieved, showing a good temporal convergence. The solution is considered converged once the normalized velocity and pressure residuals are below 1×10^{-6} and turbulent variables' residuals below 1×10^{-3}. Figure 6 shows the convergence history of the normalized residual of primitive variables pressure (P), X-velocity (U), and temperature (T). The normalized residuals are given on the Y axis as the logarithm (base 10) of the normalized residual e plotted against the number of iterations (I').

4.3 Grid Independence Study. A GCI study as proposed by Cilik et al. [44] is performed on 3 different unstructured hexahedral grids with 10,200, 34,000, and 1,177,000 elements, respectively, using the SA model. The results are given in Table 5 where the upstream reattachment length (L_{up}) as shown in Fig. 1 is taken as the parameter (ϕ) for the GCI study. The quantity L_{up} is defined as the distance from the centerline of the slot to the point on the plate surface where the separation shock would intersect the wall if extended undiminished through the boundary layer. The width of slot in the domain is set to 1 mm with $P_{\text{ratio}} = 0.31$ for the study.
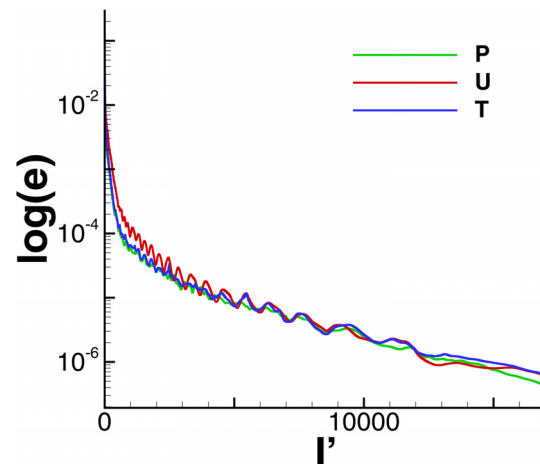

Fig. 6 Convergence history

Table 5 Grid convergence index study for transverse sonic injection in supersonic flow

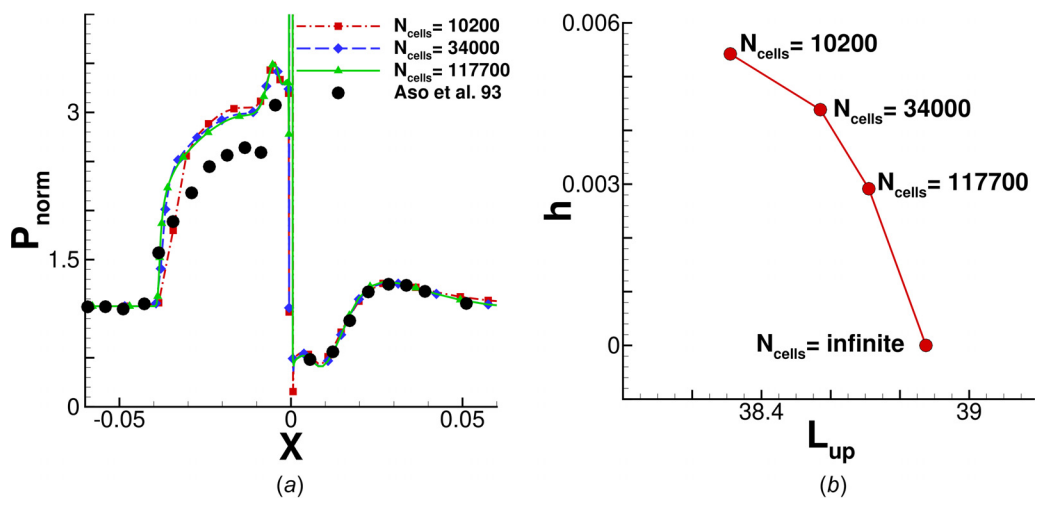| Parameter	Value
N_1, N_2, N_3	117,700, 34,000, 10,200
r_{21}	1.86
r_{32}	1.83
ϕ_1	38.71
ϕ_2	38.31
ϕ_3	38.09
p	1.984
ϕ_{ext}^{21}	38.87
e_a^{21}	1.03%
e_{ext}^{21}	0.19%
GCI^{21}	0.2%
e_a^{32}	3.57%
e_{ext}^{32}	1.45%
GCI^{32}	1.305%

Fig. 7 Results obtained from grid convergence index analysis: (a) GCI comparison of P_{norm} over plate surface and (b) Richardson extrapolation for the meshes used in GCI

Figure 7(a) shows the profile of the normalized pressure P_{norm} plotted for each of three meshes used for the GCI. Figure 7(b) compares L_{up} with $h = \sqrt{(1/N_{cells})}$. The value at $h = 0$, indicating an infinitely fine mesh ($N_{cells} = \infty$), is obtained using Richardson extrapolation.

The parameters given in Table 5 are as described in Sec. 3.1. The normalized static pressure distribution over the plate, given by Eq. (42), is plotted for all three grids and compared with the experimental results in Fig. 7(a). It is seen that the grid with 34,000 cells can be used for further computations, as it has an estimated 1.3% error. The grid has 341 nodes in the horizontal direction and 101 nodes in the vertical direction. Results from Richardson interpolation, plotted in Fig. 7(b), show a recirculation length of 38.4 for $h = 0$.

5 Results

5.1 Flow Features. As a highly underexpanded jet at sonic speed is injected in the transverse direction into the supersonic crossflow, various flow features are observed that characterize the flow field. An overview of the flow features in the jet plume is provided by the Mach number contours as shown in Fig. 8. The jet while exiting the slot tends to move parallel to the centerline of the slot width. However, as the freestream pressure is higher than the injected jet pressure, it forces the fluid to move away from the centerline. In the exit plane of the jet, the Prandtl–Meyer

expansion fan expands the fluid up to the jet boundary. These waves then turn inward into compression waves and are reflected from the constant pressure streamlines, where their pressure is equal to the ambient pressure. This barrel shock then proceeds to converge and, above a critical angle, the reflection becomes singular and leads to the appearance of a normal shock called the Mach disk and a reflected shock is produced. The point where the incident shock (barrel shock), Mach disk, and reflected shock intersect is called the triple point. The barrel shock acts as a blunt body obstruction to the incoming flow, thus creating a detached bow shock.

Inside the plume, the flow first accelerates and then is suddenly decelerated by the Mach disk that slows down the highly supersonic flow inside the plume to subsonic speeds. This subsonic flow generated by the Mach disk forms a slip surface, with the supersonic flow around and past the barrel shock. The slip surface surrounded by slip lines is clearly visible in Fig. 8. The triple point can also be easily identified. However, the reflected shock is barely identifiable due to strong interference created by the crossflow and bow shock. Figure 8 depicts the computational results obtained for a slot width of 0.5 mm for a $P_{ratio} = 0.23$.

It is seen that the computations capture all the qualitative physical features of the actual flow as seen in Fig. 1, thus confirming that the flow simulations produce physically realistic flow results, and qualitatively show all the features seen in the experiments.

Since P_{norm} is a key parameter in this study, its contours are superimposed with the flow streamlines against the P_{norm} graph in Figs. 9 and 10 to explore its different features and correlate them with the flow field.

In Fig. 9, there are two counter-rotating vortices α (from C to A') and β (from C to D'). The direction of flow in the vortices can be discerned from the higher to lower P_{norm} values in the graph. To show the β vortex clearly and mark the endpoint of the vortex between points D and E, the region from D to D' is enlarged in a subwindow in Fig. 9.

Between points A and A', a sharp increase in P_{norm} shows a high pressure gradient due to the separation shock. The upstream separation length (L_{up}) is measured by checking the sign of the X component of the velocity field at the first grid point from the injector center located at $X = 0$. It is observed that L_{up} is quite near to the point A. The slope of the P_{norm} curve changes its sign at point C, establishing it as the stagnation point between vortex regions α and β. Points B and D can be mapped to the core of the vortices α and β, respectively. The sharp drop in pressure between D' and E represents the footprint of the bow shock. Beyond point E, the sharp rise in the pressure depicts the footprint of the barrel shock at the tip of the injector inlet.
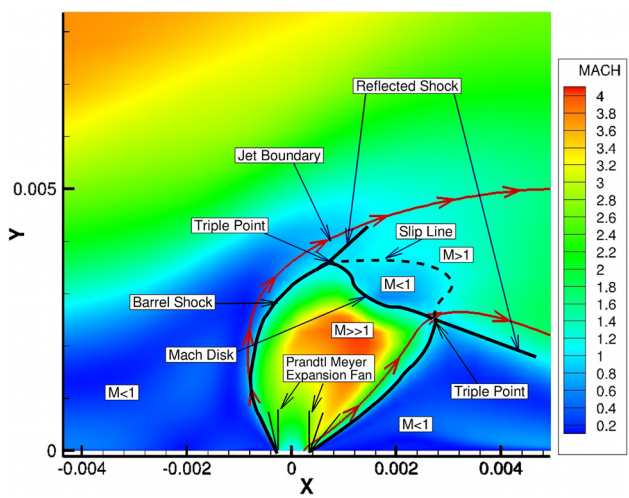

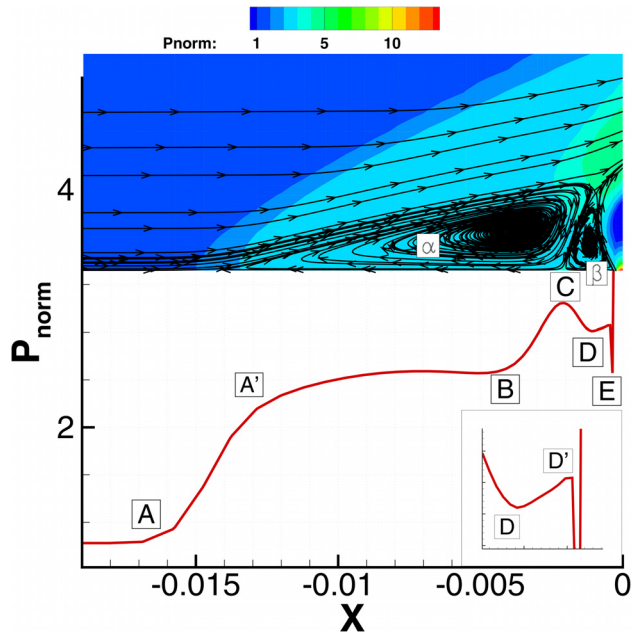Fig. 8 Flow features captured by the solver

Fig. 9 Flow field mapped against the P_{norm} graph, just ahead of the tip of the injector inlet
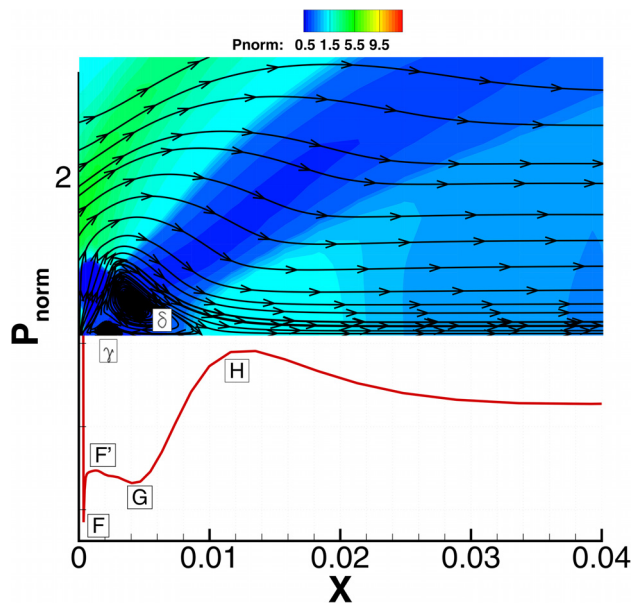

Fig. 10 Flow field mapped against the P_{norm} graph, just after the tip of the injector inlet

Figure 10 shows the flow-field downstream of the injector. Two counter-rotating vortices γ and δ are present in this region. The barrel shock is captured at the tip of the injector inlet at point F, and the reflected shock foot-print is captured by the region between F and F'. Point G is the stagnation point between the two vortices. The streamlines then gradually adjust themselves to become parallel to the flat plate, as the value of P_{norm} gradually approaches one in the graph.

5.2 Two-Dimensional Simulations. In the experimental study, two slots of width (W) 0.5 mm and 1 mm were used. For each case, experiments were performed for six different pressure ratios (P_{ratio}) of 0.077, 0.15, 0.23, 0.31, 0.37, and 0.46. The 2D simulations that are presented in this section are performed using the SA and SST models.

5.2.1 Effect of Compressibility Correction. Shocks cause increased dissipation of turbulence not accounted for by the standard Kolmogorov cascade dissipation rate. This additional dissipation of the turbulence can be modeled by compressibility corrections included in the governing equations of the turbulent models. Hence, the computations were also done using the compressibility correction (*CC*) (Eq. (34)) for the SA and SST models, as described in Sec. 2.3.

On comparing the P_{norm} profile with and without compressibility correction, as shown in Fig. 11, it is observed that the P_{norm} profile remains essentially unchanged after including the compressibility correction for the SST model but in the SA results there is a discernible change.

The upstream separation length (L_{up}) is measured by checking the change in the sign of the X component of the velocity field at the first grid point away from the wall. Upon comparing different results in Fig. 12, it is observed that the compressibility correction possibly enhances the accuracy of solution for the SA model but, as the uncertainty in the experimental dataset has not been provided by Aso et al. [7], it is difficult to exactly quantify the improvement. For the SST model, L_{up} is still overpredicted and no change is observed in the results due to the compressibility corrections, as seen in Fig. 12. As no improvement is observed, L_{up} for SST model with the compressibility correction has not been plotted in Fig. 12.

In the SST model, the compressibility correction is dependent on the local turbulent Mach number (M_t). Since its maximum value is found quite small ($\approx 1 \times 10^{-3}$), this makes the SST model insensitive to the compressibility correction. The compressibility correction in the SA model is dependent on the magnitude of the velocity gradients in the flow field, as seen in Eq. (34). In the flow field under investigation, especially in the region near the jet inlet, the gradients of velocity are quite high due to the presence of multiple shock structures, as seen in Figs. 9 and 10. Hence, the contribution of the added dissipation term is significant, which can be seen in the results through a decrease in the value of L_{up} in Fig. 12.

5.2.2 Effect of Corrections for Turbulence Production. It has been previously mentioned that the presence of stagnation points leads to the overestimation of the turbulence production P_k. To account for this overestimation, various corrections have been discussed in Sec. 2.2.3 for both the SA and SST models. These corrections are now assessed in order to see if any change is observed in the results computed using them. The comparisons have been done for the numerical simulation for $P_{ratio} = 0.23$ for a slot width of 0.5 mm.

In Fig. 13(*a*), the SA-STBLI correction given by Eq. (33) is implemented in the model and the results compared with the previous results with compressibility correction in which it is observed that there is no change in the P_{norm} profile. The SA model with the compressibility correction (but not the STBLI correction) shall now be used to compare the results with the experimental data of Aso et al. [7], as it gives a better prediction of L_{up}.

In Fig. 13(*b*), different corrections in P_k for regions of flow separation, that have been proposed for the SST model and have been described in Sec. 2.2.3, are compared. It is seen that none of the corrections change the results significantly, except for the STBLI correction given by Eq. (27). This shows that for the SST model, the effect of boundary layer separation due to STBLI should be modeled in order to correctly predict the L_{up} and the P_{norm} profile, while the other corrections have negligible effects.

Hence, the experimental data from Aso et al. [7] shall be compared only with and without the STBLI correction in the SST model, i.e., without compressibility correction, in order to assess its overall performance.

5.3 Comparison of Two-Dimensional Simulation Results With the Experimental Results. Upon comparing the results in Figs. 14 and 15, it is observed that the SST model overpredicts the P_{norm}, which strongly diverges from the experiments. The discrepancy in the results increases with the increase in P_{ratio}. On the
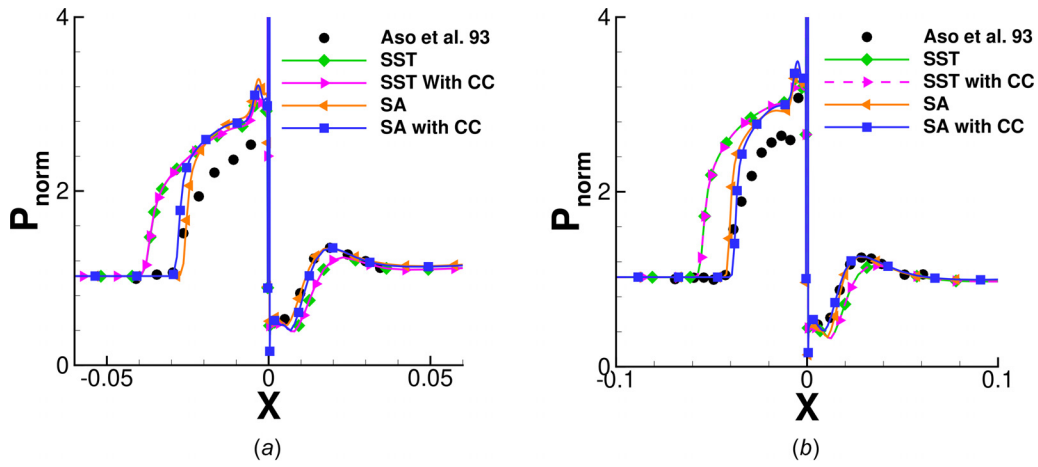
Fig. 11 Comparison of $P_{ratio} = 0.31$ with and without compressibility correction for the SA and SST models: (a) 0.5 mm and (b) 1 mm
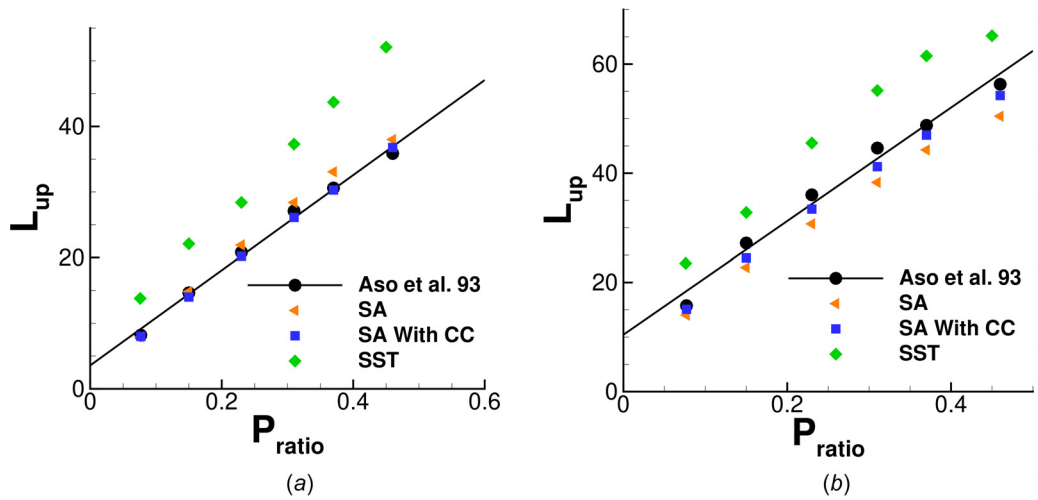

Fig. 12 Comparison of L_{up} with and without compressibility correction (where CC denotes compressibility correction) for the SA and SST models: (a) 0.5 mm and (b) 1 mm
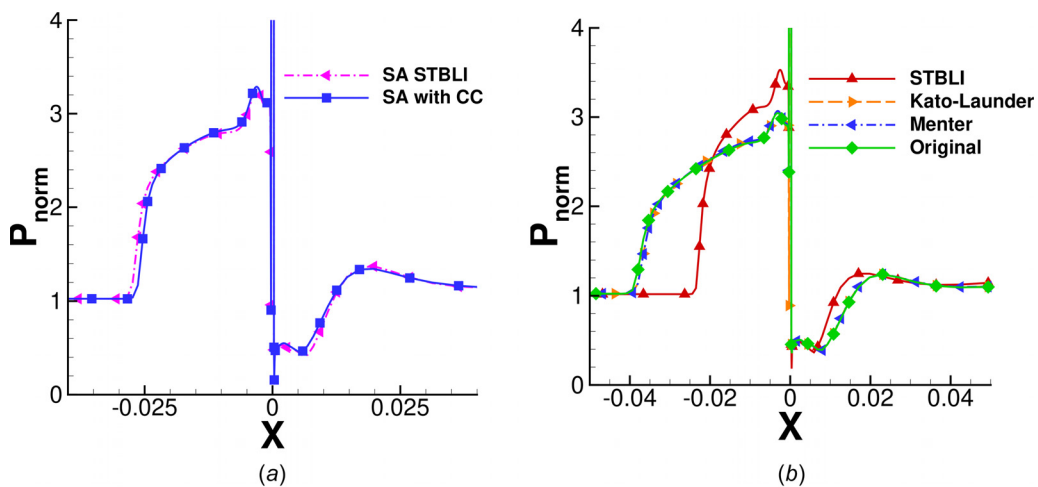

Fig. 13 Comparison of different corrections for SA and SST models for STBLI: (a) SA model correction and (b) SST model corrections
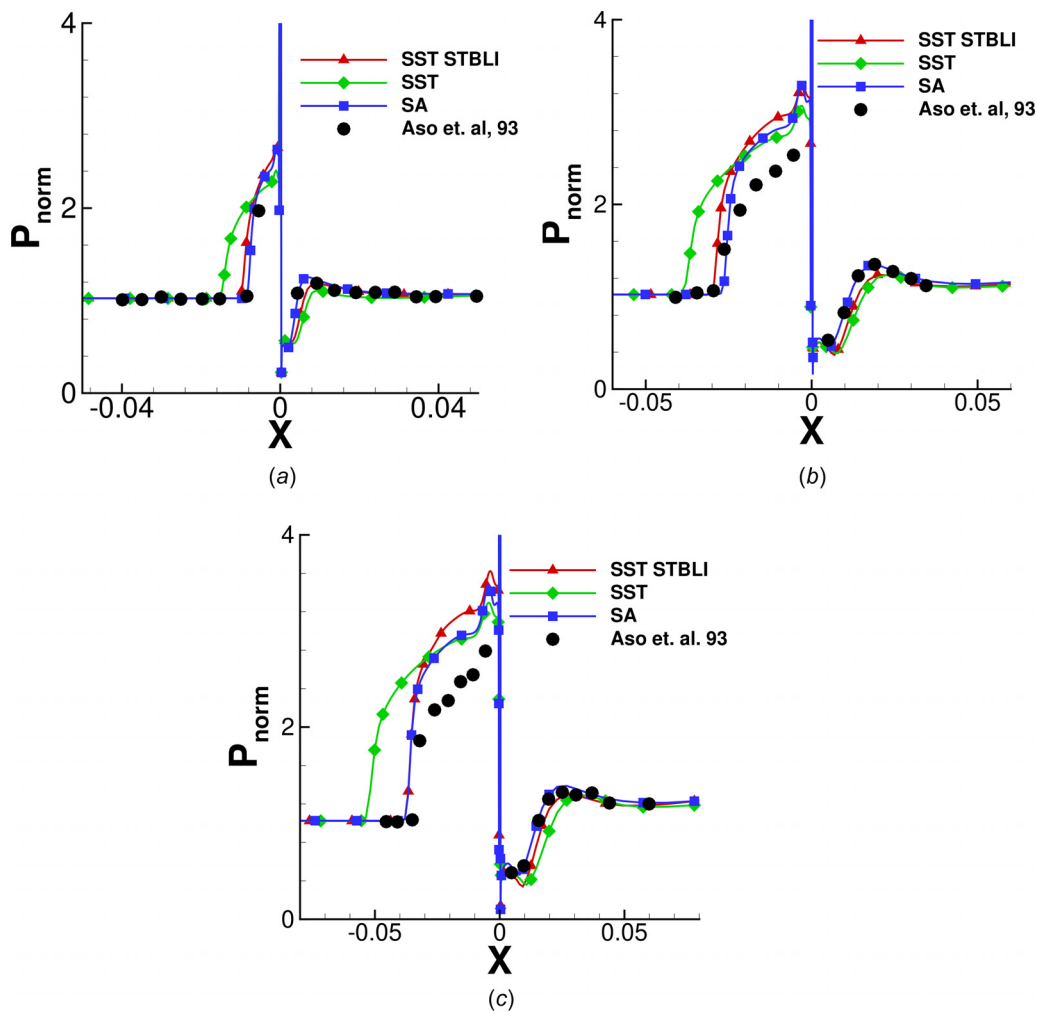
Fig. 14 Comparison of experimental and numerical data for different RANS models for slot width = 0.5 mm: (*a*) P_{ratio} = 0.077, (*b*) P_{ratio} = 0.31, and (*c*) P_{ratio} = 0.46

other hand, SA model seems to predict the P_{norm} profiles quite well when compared to the SST model. Upon using the SST-STBLI model, the results match those obtained from SA model and are quite close to the experiments.

It should be noted that Huang et al. [14] and Sriram and Mathew [13,51] observed similar overprediction at these pressure ratios by the SST model. It is evident that using the STBLI turbulence production with the SST model significantly improves the results. Also, a better match is obtained with lower values of P_{ratio} for the current dataset. However, numerical results obtained for the same dataset using the k–ϵ model by Rizetta [11] and Clark and Chan [52] and the Reynolds stress model by Chenault and Beran [12] produce a similar pressure jump in the P_{norm} profiles. The parameter L_{up} obtained by these models also show similar differences with the experimental results. It can be noted that the computed peak pressure is higher than the experimental values in all the cases. Similar trends have been observed by other researchers [11], who speculated that this discrepancy is possibly due to flow leakage from the lateral edge of the slot that would have occurred in the experiments (which will not be captured by the 2D simulations). In order to investigate the validity of this explanation, three-dimensional computations simulating the condition with no fence around the slot are performed and discussed in Secs. 5.4–5.7.

5.4 Three-Dimensional Simulations. The computations in Secs. 5.2 and 5.3 were performed assuming two-dimensionality. It is observed that the P_{norm} values downstream of the transverse jet

outlet, where the flow is subsonic, match well with the experimental results for different slot widths and pressure ratios for all the tested models. However, upstream of the transverse jet, while the P_{norm} profiles show the trends similar to the experiments, the models overpredict the P_{norm} profiles of the two-dimensional dataset. Similar overprediction has been seen by several other researchers for simulations using different RANS models [11,12,14,15,51,52]. The reason for this has been attributed by Rizetta [11] to be due to the pressure relief in the experimental data caused by the spillage from the spanwise edge of the experimental slot. It has been argued by Rizetta [11] that an increase in P_{ratio} leads to more spillage increasing the disparity between the experimental and the numerical result, as is observed. However, this claim was not confirmed by actual computations by any of the aforementioned authors [11,12,14,15,51,52] who have seen similar overpredictions.

Hence, we check for this possibility using two methods. In the first method, case 1, the slot is extended from end to end across the lateral width of the domain. This implies that in case 1, the three-dimensional computation can include possible 3D flow structures but does not aim to replicate the actual 3D geometrical setup used in the experiments. In the second case, case 2, the slot is reduced to be of finite length inside the domain, as shown in Fig. 17 and so simulates the actual 3D experiment.

5.5 Grid Convergence Index for Three-Dimensional Computations. The current computational domain for a slot-width of 0.5 mm was extended to 130 mm in the *z* direction. In order to
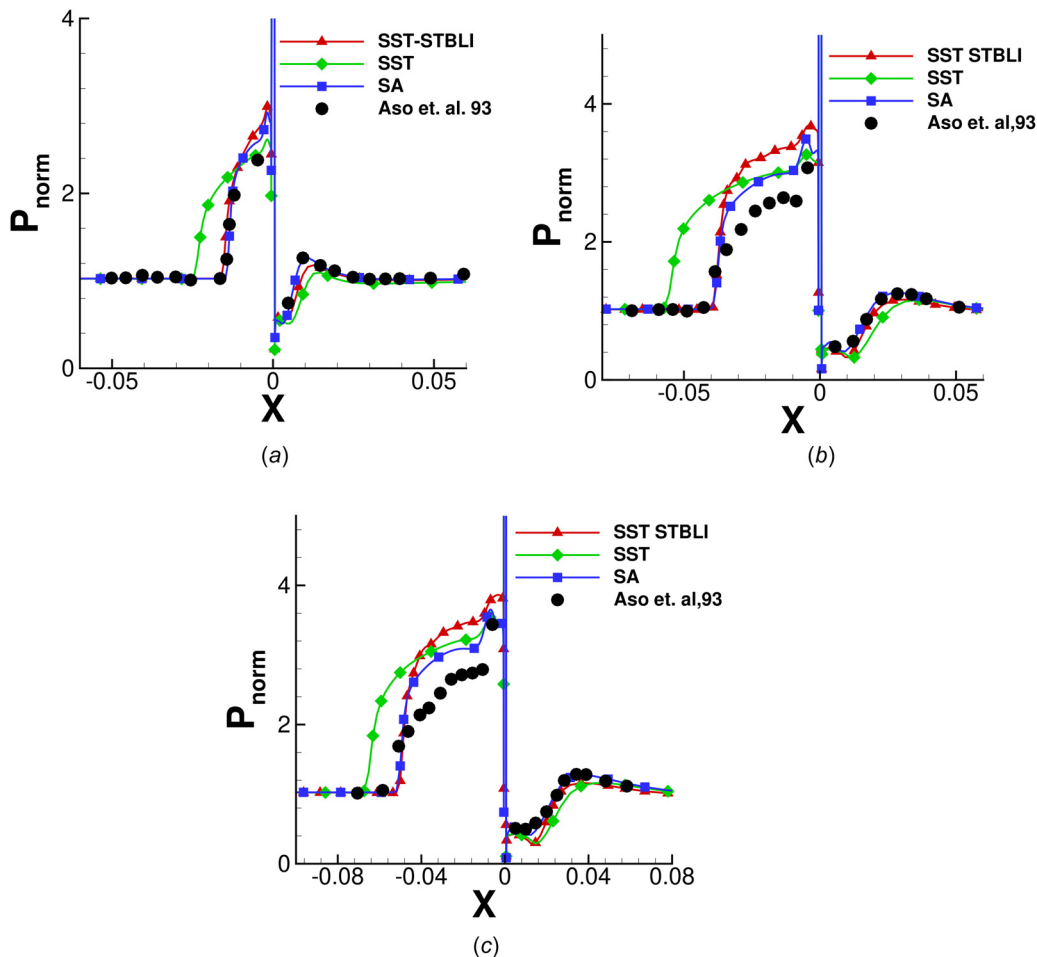
Fig. 15 Comparison of experimental and numerical data for different RANS models for slot width = 1 mm: (a) P_{ratio} = 0.077, (b) P_{ratio} = 0.31, and (c) P_{ratio} = 0.46
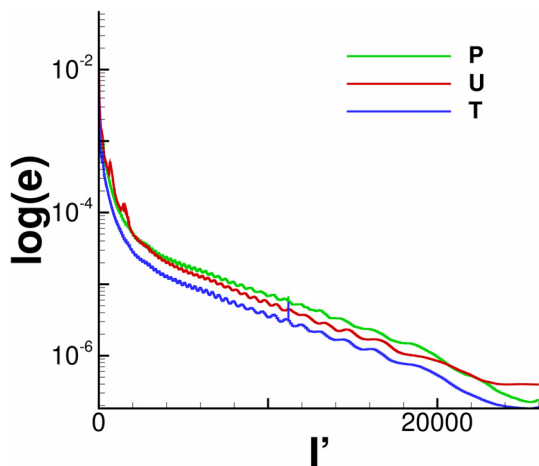
Fig. 16 Convergence history

establish mesh sensitivity, GCI was performed on 3 meshes of size 1,020,000, 295,494, and 86,047, respectively, using the SA model for case 2. The parameter L_{up} has been taken as the parameter for GCI and the simulations were done without the STBLI correction for a P_{ratio} = 0.23. The boundary conditions remained same as in the previous simulations but with symmetry being additionally used in the third direction boundaries. Explicit time stepping with CFL numbers ranging from 0.1 to 0.3 are taken for the simulations. For all the simulated CFL numbers between 0.1 and 0.3, the same P_{norm} profile is achieved, showing a good temporal convergence. The solution is considered converged once the velocity and pressure residuals are below 1×10^{-6} and turbulent variables' residuals below 1×10^{-3}. Figure 6 shows the convergence history of the normalized residual of the primitive variables pressure (P), X-velocity (U), and temperature (T). The normalized residuals are given on the Y axis as the logarithm (base 10) of the normalized residual e plotted against the number of iterations (I') on the X axis. Using these computational conditions, the results have been tabulated in Table 6 and Fig. 16.

Based on the GCI, the finest mesh with 1,020,000 hexahedral elements and estimated error of 4.24% has been used for further study.

5.6 Comparison Between Cases 1 and 2. In order to compare case 1 with case 2, the boundary conditions as mentioned in Sec. 5.5 have been used. Validation against the experimental results is shown in Fig. 18.

The results obtained for case 1 are shown in Fig. 18(a). It should be noted that only SA model has been simulated for this case for a P_{ratio} of 0.077. It can be observed that there is no change in the P_{norm} profile. So, it seems unlikely that the earlier results would be affected by purely flow structure three-dimensionality that would be captured in case 1.

In order to make the flow fields 2D, "aerodynamic fences" were used by Aso et al. [7] in their experiments. The 2D results that have been presented above have been compared against the experimental results with the aerodynamic fence. But for case 2, the
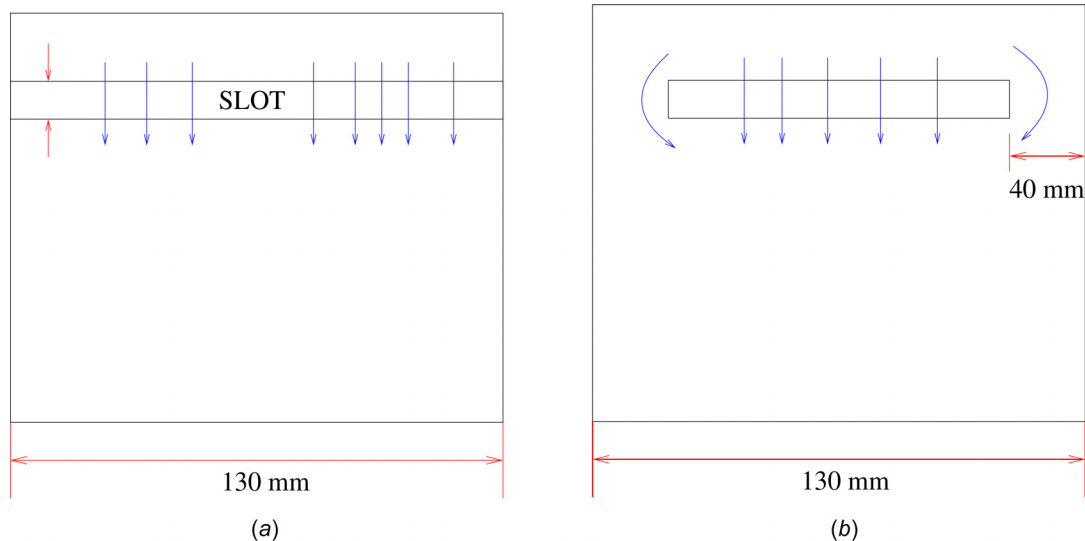
Fig. 17 Slot width and length of domain in the *Z* direction for 3D simulations. Note that only the section of plate with slot is shown: (*a*) case 1 and (*b*) case 2.

Table 6 Grid convergence index study for case 2

Parameter	Value
N_1, N_2, N_3	1,020,000, 295,494, 86,047
r_{21}	1.511
r_{32}	1.508
ϕ_1	18.844
ϕ_2	17.952
ϕ_3	16.732
p	2.116
ϕ_{ext}^{21}	19.48
e_a^{21}	4.73%
e_{ext}^{21}	3.28%
GCI^{21}	4.24%
e_a^{32}	6.79%
GCI^{32}	6.12%

computed results are compared against the 3D experimental data of Aso et al. [7] obtained without the aerodynamic fence. In Fig. 18(*b*), we assess the SA, SST, and SST-STBLI models. We see that an excellent match has been obtained against the experimental results for P_{norm} with the SA and the SST-STBLI model. As evident from Fig. 18(*b*), the SST model overpredicts L_{up} and does not predict P_{norm} as closely as the SA model. Upon using the SST-STBLI, the result is much closer to the experimental result and quite close to the SA model. This offers very compelling evidence that the overshoot of the pressure seen in the 2D results is caused by the leakage from the lateral edges of the slot in the experiments that is unaccounted for in the 2D simulations. The closer results in case 2 suggest that "fences" in the experiments did not make the flow truly 2D. This explains the discrepancies in the pressure predictions found in this and previous studies.

5.7 Comparison of Flow Features. Figure 19 shows the comparison of P_{norm} for an infinite slot length using a three-dimensional grid as shown in Fig. 17(*a*) and simulation with a finite length slot with as shown in Fig. 17(*b*) for the SA model and
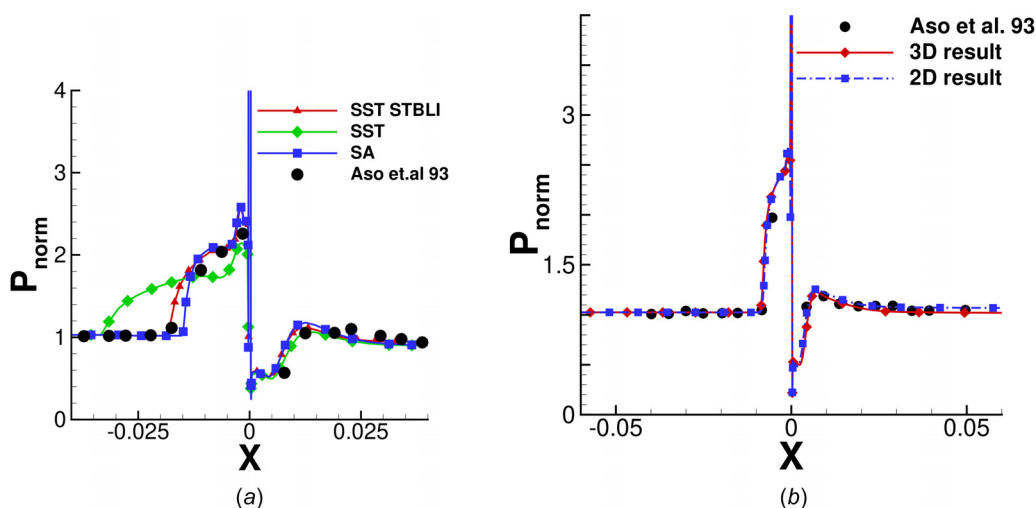

Fig. 18 Validation against experimental results for cases 1 and 2: (*a*) case 1: comparison of P_{norm} profiles between 2D and 3D simulations for $P_{ratio} = 0.077$ and (*b*) case 2: validation of P_{norm} against experimental results for $P_{ratio} = 0.23$ for different RANS models
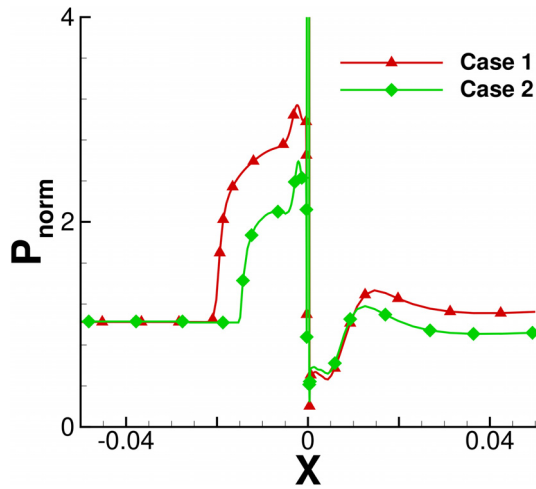
Fig. 19 Comparison of P_{norm} between infinite and finite length slot as shown in Fig. 17 simulations for P_{ratio} =0.23 for SA model
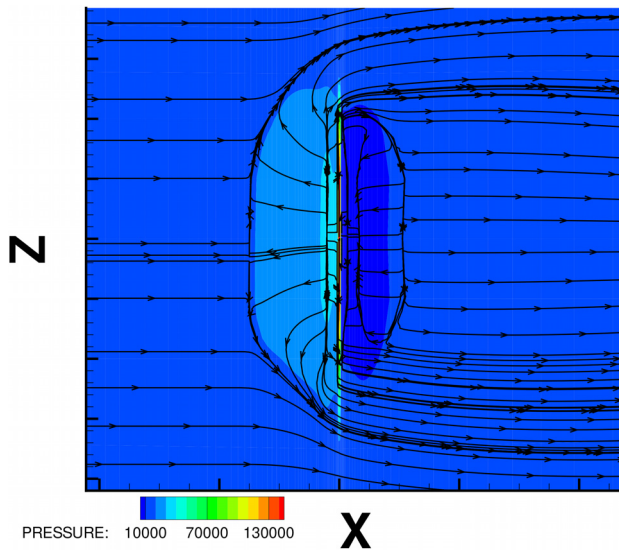

Fig. 20 Streamlines over the plate surface ($Y = 0$ plane) around the finite slot with pressure contours

$P_{ratio} = 0.23$. It can be seen that the graphs are similar in shape, meaning that no additional flow structure was created by the three-dimensionality. However, there is a significant shift in the key points A and H, which are, respectively, defined in Figs. 9 and 10.

It is also evident that L_{up} for the finite slot length case is smaller than the infinite (2D) slot length case, as evident by the shift of point A toward the injector. It should be noted that the stagnation point C remains at the same position. This decrease in length of L_{up} can be attributed to the finite length of the slot, which allows the fluid to move around the slot (as shown in Fig. 20) and merge in the flow field downstream of the injector. The 3D nature of the flow field also decreases the strengths of the shocks, as evident from the decrease in values of peak P_{norm}, before and after the injector. This movement of fluid around the injector creates a relief effect in the flow field, allowing the fluid to move and reduce the size of the upstream recirculation zone. Due to this relief effect in the downstream of the injector, a shift in point H is noted. This shift shows that the value of pressure renormalization is lower for the finite (3D) slot than that of the infinite (2D) slot. It can be seen from Fig. 19 that the qualitative shape of the graphs

irrespective of their values remains same, hence no new recirculation zone is formed. Even the slope of the two P_{norm} graphs is almost identical. However, this turning of the flow around the slot leads to the formation of various vortices, the details of which we hope to discuss in another paper.

6 Conclusions

The validity of the SA and SST models for applications in the underexpanded jets injected into a supersonic crossflow is investigated in this paper using an in-house parallel RANS solver. Further, several corrections that have been proposed in the literature for both the SA and SST models in the flows involving regions of flow separation have been assessed in this paper. Grid independence of the results is demonstrated using the GCI parameter. Two-dimensional simulations were done to compare against the data provided by the experiments of Aso et al. [7]. The upstream separation length (L_{up}) is captured successfully by the SA model and the compressibility correction is seen to affect the separation length, whereas in the P_{norm} results its effect is seen to be marginal. In case of the SST model, both these results are overpredicted. The SST model is found insensitive to the compressibility corrections. The correction in the turbulence production P_k due to the presence of stagnation points does not play a significant as compared to modeling the effects of STBLI in the SST model. We see that only the STBLI correction by Sinha et al. [27] when applied to the SST model produces a significant (and positive) change in the results. The SA model is found to be insensitive to the Sinha et al. [27] STBLI correction. It is seen that upon using the SST-STBLI, the SST results were quite close to the SA model results (which are closer to the experiments).

A mismatch in the results and experiments is observed in the flow upstream of the transverse jet. Researchers have suggested some effect of three-dimensionality [11,12,52] in these experiments. In order to confirm this, three-dimensional simulations were also performed using the SA, SST, and SST-STBLI models. The results from these simulations have been matched with the second (3D) dataset of the experiments (obtained without any aerodynamic fences that the experimenters believed would make the flow 2D). It is observed that a reasonable match is produced with the experimental results. This suggests that it is highly likely that the pressure overprediction in the 2D simulations in this and previous studies was due to the experiments not being rendered fully 2D by the fences used.

This study demonstrates that the RANS models accurately predict both L_{up} and the pressure, apart from accurately capturing the general features of the entire flow as seen in Sec. 5.1. The SA model is able to successfully obtain L_{up} and P_{norm} for the 3D dataset of Aso et al. [7], which has shock-boundary layer interaction. This shows that this one-equation model is surprisingly successful in capturing these parameters at a fraction of the computational cost of large eddy simulations at least for the dataset of Aso et al. [7]. The SA model generally performs even better than the two-equation SST model in predicting these flow features. The SST model gives a good prediction (close to SA and the experiments) only when the STBLI corrections of Sinha et al. [27] are used.

Nomenclature

a = speed of sound
A_f = area of a face of a cell in mesh
C_f = skin friction coefficient
C_p = specific heat at constant pressure
e = absolute error
E = total energy per unit mass
e_a = absolute error between two meshes
h = specific enthalpy of the gas
H = total enthalpy per unit mass
I = turbulence intensity
I' = number of iterations
k = turbulent kinetic energy
k' = thermal conductivity of gas

L_{up} = upstream reattachment length
M_t = turbulent Mach number
M_∞ = freestream Mach number
N = number of cells in the mesh
p = local order of accuracy
P = static pressure of gas
P_k = turbulence production
P_{norm} = ratio of static pressure at wall surface to freestream static pressure
P_{ratio} = ratio of static pressure at jet inlet to freestream static pressure
$P_{\tilde{\nu}}$ = production of turbulent eddy viscosity
P_w = pressure at wall surface
P_0 = total pressure of gas
$\mathbf{q}$ = heat flux tensor
Re = Reynolds number
S_{ij} = strain rate tensor
T = static temperature of gas
T_w = temperature at wall surface
$u+$ = dimensionless velocity parallel to the wall as a function of distance from the wall
$\tilde{\nu}$ = eddy viscosity
$\mathbf{V}$ = velocity vector = $u\hat{\mathbf{i}} + v\hat{\mathbf{j}} + w\hat{\mathbf{k}}$
W = width of the slot
W_{ij} = rotation rate tensor
$y+$ = dimensionless distance y to the wall
Y_C = compressibility correction
Γ = ratio of specific heats of a gas
Δt = time-step
ϵ = turbulent dissipation
λ = coefficient of bulk viscosity
μ = dynamic viscosity of fluid
μ_t = turbulent dynamic viscosity of fluid
ν = kinematic viscosity of fluid
ρ = density of gas
τ_{ij} = Reynold's stress tensor
ϕ = parameter for GCI
Ω = magnitude of vorticity
ω = turbulent

References

[1] Srinivasan, R., and Bowersox, R., 2005, "Assessment of RANS and DES Turbulence Models for Supersonic Jet Interaction Flows," AIAA. Paper No. 2005-499

[2] Won, S.-H., Jeung, I.-S., Parent, B., and Choi, J.-Y., 2010, "Numerical Investigation of Transverse Hydrogen Jet Into Supersonic Crossflow Using Detached-Eddy Simulation," AIAA J., 48(6), pp. 1047–1058.

[3] Kawai, S., and Lele, S. K., 2010, "Large-Eddy Simulation of Jet Mixing in Supersonic Crossflows," AIAA J., 48(9), pp. 2063–2083.

[4] Peterson, D. M., and Candler, G. V., 2010, "Hybrid Reynolds-Averaged and Large-Eddy Simulation of Normal Injection Into a Supersonic Crossflow," J. Propul. Power, 26(3), pp. 533–544.

[5] Thornber, B., and Drikakis, D., 2007, "Large-Eddy Simulation of Shock-Wave-Induced Turbulent Mixing," ASME J. Fluids Eng., 129(12), pp. 1504–1513.

[6] Chakraborty, D., Roychowdhury, A., Ashok, V., and Kumar, P., 2003, "Numerical Investigation of Staged Transverse Sonic Injection in Mach 2 Stream in Confined Environment," Aeronaut. J., 107(1078), pp. 719–729.

[7] Aso, S., Okuyama, S., Ando, Y., and Fujimori, T., 1993, "Two-Dimensional and Three-Dimensional Mixing Flow Fields in Supersonic Flow Induced by Injected Secondary Flows Through Traverse Slot and Circular Nozzle," AIAA Paper No. 1993-489.

[8] Huang, W., and Yan, L., 2013, "Progress in Research on Mixing Techniques for Transverse Injection Flow Fields in Supersonic Crossflows," J. Zhejiang Univ. Sci. A, 14(8), pp. 554–564.

[9] Huang, W., 2016, "Transverse Jet in Supersonic Crossflows," Aerosp. Sci. Technol., 50, pp. 183–195.

[10] Huang, W., 2018, "Mixing Enhancement Strategies and Their Mechanisms in Supersonic Flows: A Brief Review," Acta Astronaut., 145, pp. 492–500.

[11] Rizetta, D. P., 1992, "Numerical Simulation of Slot Injection Into a Turbulent Supersonic Stream," AIAA J., 30(10), pp. 2434–2439.

[12] Chenault, C. F., and Beran, P. S., 1998, "K-Epsilon and Reynolds Stress Turbulence Model Comparisons for Two-Dimensional Injection Flows," AIAA J., 36(8), pp. 1401–1412.

[13] Sriram, A., and Mathew, J., 2006, "Improved Prediction of Plane Transverse Tets in Supersonic Crossflows," AIAA J., 44(2), pp. 405–408.

[14] Huang, W., Liu, W.-D., Li, S.-B., Xia, Z.-X., Liu, J., and Wang, Z.-G., 2012, "Influences of the Turbulence Model and the Slot Width on the Transverse Slot Injection Flow Field in Supersonic Flows," Acta Astronaut., 73, pp. 1–9.

[15] Yan, L., Huang, W., Li, H., and Zhang, T.-T., 2016, "Numerical Investigation and Optimization on Mixing Enhancement Factors in Supersonic Jet-to-Crossflow Flow Fields," Acta Astronaut., 127, pp. 321–325.

[16] Desikan, S., Saravanan, R., Subramanian, S., Sivararamakrishnan, A., and Pandian, S., 2015, "Investigation of Supersonic Jet Interaction With Hypersonic Cross Flow," ASME J. Fluids Eng., 137(10), p. 101101.

[17] Hariharan, A. R., and Babu, V., 2014, "Transverse Injection Into a Supersonic Cross Flow Through a Circular Injector With Chevrons," ASME J. Fluids Eng., 136(2), p. 021204.

[18] Kumar, S. A., and Rathakrishnan, E., 2017, "Nozzle Aspect Ratio Effect on Supersonic Elliptic Jet Mixing," ASME J. Fluids Eng., 139(10), p. 101103.

[19] Huang, W., 2014, "Design Exploration of Three-Dimensional Transverse Jet in a Supersonic Crossflow Based on Data Mining and Multi-Objective Design Optimization Approaches," Int. J. Hydrogen Energy, 39(8), pp. 3914–3925.

[20] Huang, W., Li, L.-Q., Chen, X.-Q., and Yan, L., 2017, "Parametric Effect on the Flow and Mixing Properties of Transverse Gaseous Injection Flow Fields With Streamwise Slot: A Numerical Study," Int. J. Hydrogen Energy, 42(2), pp. 1252–1263.

[21] Spalart, P., and Allmaras, S., 1992, "A One-Equation Turbulence Model for Aerodynamic Flows," AIAA Paper No. 1992-439.

[22] Deck, S., Duveau, P., d'Espiney, P., and Guillen, P., 2002, "Development and Application of Spalart–Allmaras One Equation Turbulence Model to Three-Dimensional Supersonic Complex Configurations," Aerosp. Sci. Technol., 6(3), pp. 171–183.

[23] Menter, F. R., 1994, "Two-Equation Eddy-Viscosity Turbulence Models for Engineering Applications," AIAA J., 32(8), pp. 1598–1605.

[24] Menter, F. R., 2009, "Review of the Shear-Stress Transport Turbulence Model Experience From an Industrial Perspective," Int. J. Comput. Fluid Dyn., 23(4), pp. 305–316.

[25] Kato, M., and Launder, B. E., 1993, "The Modelling of Turbulent Flow Around Stationary and Vibrating Square Cylinders," Proceedings of Ninth Symposium on Turbulent Shear Flows, Vol. 1, Kyoto, Japan, Aug. 13–16, pp. 1–6.

[26] Chung, K.-M., 2001, "Investigation on Turbulent Expansion-Corner Flow With Shock Impingement," ASME J. Fluids Eng., 123(1), pp. 139–144.

[27] Sinha, K., Mahesh, K., and Candler, G. V., 2003, "Modeling Shock Unsteadiness in Shock/Turbulence Interaction," Phys. Fluids, 15(8), pp. 2290–2297.

[28] Pathak, U., Roy, S., and Sinha, K., 2018, "A Phenomenological Model for Turbulent Heat Flux in High-Speed Flows With Shock-Induced Flow Separation," ASME J. Fluids Eng., 140(5), p. 051203.

[29] Sinha, K., Mahesh, K., and Candler, G. V., 2005, "Modeling the Effect of Shock Unsteadiness in Shock/Turbulent Boundary-Layer Interactions," AIAA J., 43(3), pp. 586–594.

[30] Sharma, V., Assam, A., and Eswaran, V., 2016, "Development of All Speed Three Dimensional Computational Fluid Dynamics Solver for Unstructured Grids," Sixth International and 43rd National Conference on Fluid Mechanics and Fluid Power (FMFP), Allahabad, India, Dec. 15–17, pp. 15–17.

[31] Weiss, J. M., and Smith, W. A., 1995, "Preconditioning Applied to Variable and Constant Density Flows," AIAA J., 33(11), pp. 2050–2057.

[32] White, F. M., and Corfield, I., 2006, Viscous Fluid Flow, Vol. 3, McGraw-Hill, New York, pp. 67–73.

[33] Weiss, J. M., Maruszewski, J. P., and Smith, W. A., 1999, "Implicit Solution of Preconditioned Navier-Stokes Equations Using Algebraic Multigrid," AIAA J., 37(1), pp. 29–36.

[34] Roe, P. L., 1981, "Approximate Riemann Solvers, Parameter Vectors, and Difference Schemes," J. Comput. Phys., 43(2), pp. 357–372.

[35] Venkatakrishnan, V., 1993, "On the Accuracy of Limiters and Convergence to Steady State Solutions," AIAA Paper No. 1993-880.

[36] Venkatakrishnan, V., 1995, "Convergence to Steady State Solutions of the Euler Equations on Unstructured Grids With Limiters," J. Comput. Phys., 118(1), pp. 120–130.

[37] Lynn, J. F., 1995, "Multigrid Solution of the Euler Equations With Local Preconditioning," Ph.D. thesis, University of Michigan, Ann Arbor, MI.

[38] Blazek, J., 2015, Computational Fluid Dynamics: Principles and Applications, Chap. 6, Butterworth-Heinemann, Oxford, UK, pp. 173–174.

[39] Sarkar, S., Erlebacher, G., Hussaini, M. Y., and Kreiss, H. O., 1991, "The Analysis and Modelling of Dilatational Terms in Compressible Turbulence," J. Fluid Mech., 227, pp. 473–493.

[40] Paciorri, R., and Sabetta, F., 2003, "Compressibility Correction for the Spalart-Allmaras Model in Free-Shear Flows," J. Spacecr. Rockets, 40(3), pp. 326–331.

[41] Sarkar, S., and Lakshmanan, B., 1991, "Application of a Reynolds Stress Turbulence Model to the Compressible Shear Layer," AIAA J., 29(5), pp. 743–749.

[42] Sarkar, S., 1992, "The Pressure–Dilatation Correlation in Compressible Flows," Phys. Fluids A: Fluid Dyn., 4(12), pp. 2674–2682.

[43] Wilcox, D. C., 1992, "Dilatation-Dissipation Corrections for Advanced Turbulence Models," AIAA J., 30(11), pp. 2639–2646.

[44] Celik, I. B., Ghia, U., and Roache, P. J., 2008, "Procedure for Estimation and Reporting of Uncertainty Due to Discretization in CFD Applications," ASME J. Fluids Eng., 130(7), p. 078001.

[45] Carlson, J., 1998, "Prediction of Very High Reynolds Number Compressible Skin Friction," AIAA Paper No. 1998-2880.

[46] Schoenherr, K. E., 1932, "Resistance of Flat Surfaces Moving Through a Fluid," Trans. Soc. Nav. Archit. Mar. Eng., **40**, pp. 279–313.

[47] Coles, D., 1956, "The Law of the Wake in the Turbulent Boundary Layer," J. Fluid Mech., **1**(2), pp. 191–226.

[48] White, F. M., and Corfield, I., 2006, *Viscous Fluid Flow*, Vol. 3, McGraw-Hill, New York, p. 496.

[49] White, F. M., and Corfield, I., 2006, *Viscous Fluid Flow*, Vol. 3, McGraw-Hill, New York, p. 548.

[50] Sutherland, W., 1893, "The Viscosity of Gases and Molecular Force," London, Edinburgh, Dublin Philos. Mag. J. Sci., **36**(223), pp. 507–531.

[51] Sriram, A., and Mathew, J., 2004, "Numerical Prediction of Two-Dimensional Transverse Injection Flows," AIAA Paper No. 2004-1099.

[52] Clark, S., and Chan, S., 1992, "Numerical Investigation of a Transverse Jet for Supersonic Aerodynamic Control," AIAA Paper No. 1992-639.